



## Interannual forcing mechanisms of California Current transports II: Mesoscale eddies

Andrew Davis, Emanuele Di Lorenzo

School of Earth and Atmospheric Science, Georgia Institute of Technology, 311 First Drive Atlanta, GA 30332-0340, USA



### ARTICLE INFO

Available online 20 February 2014

**Keywords:**

Eastern Boundary Currents  
California Current  
Transport processes  
Mesoscale eddies  
Wind stress curl

### ABSTRACT

Mesoscale eddies exert dominant control of cross-shelf exchanges, yet the forcing dynamics underlying their interannual and decadal variability remain uncertain. Using an ensemble of high-resolution ocean model hindcasts of the central and eastern North Pacific from 1950 to 2010 we diagnose the forcing mechanisms of low-frequency eddy variability in the California Current System (CCS).

We quantify eddy activity by developing eddy counts based on closed contours of the Okubo-Weiss parameter and find that the spatial and temporal features of model-derived counts largely reproduce the short AVISO observational record.

Comparison of model ensemble members allows us to separate the intrinsic and deterministic fractions of eddy variability in the northern CCS ( $34.5\text{--}50^\circ\text{N}$ ) and in the southern CCS ( $28.5\text{--}34.5^\circ\text{N}$ ). In the North, a large fraction of low-frequency eddy variability (30% anticyclones, 20% cyclones) is deterministic and shared with satellite observations. We develop a diagnostic model based on indices of the large-scale barotropic and baroclinic states of the CCS which recovers this deterministic variance. This model also strongly correlates with local atmospheric forcing. In contrast to the North, Southern CCS eddy counts exhibit very little deterministic variance, and eddy formation closely resembles a red-noise process.

This new understanding of the external forcings of eddy variability allows us to better estimate how climate variability and change impact mesoscale transports in the California Current. The skill of our diagnostic model and its close association with local wind stress curl indicate that local atmospheric forcing is the dominant driver of eddy activity on interannual and decadal time scales north of pt. conception ( $\sim 33^\circ\text{N}$ ).

© 2014 Elsevier Ltd. All rights reserved.

### 1. Introduction

The California Current System (CCS) is the Eastern Boundary Current (EBC) associated with the Northern Pacific Subtropical Gyre. It is a region of strong biological productivity, due in large part to seasonal wind-driven nutrient upwelling (Hickey, 1998). While it displays physical variability on virtually all spatial and temporal scales, eddy scale variance is particularly strong (Marchesiello et al., 2003). Eddies play a large role in local horizontal and vertical mixing, and their nonlinearity effectively entrains and transports physical and biological tracers offshore (Chereskin et al., 2000; Cornuelle et al., 2000; Gruber et al., 2006; Combes et al., 2013). CCS eddies may also contribute to the generation of Eastern boundary subsurface temperature and salinity anomalies, which have been shown to propagate into the

equatorial thermocline (Fukumori et al., 2004), possibly feeding back onto the climate system. While CCS eddy formation is a chaotic process and therefore to a large extent intrinsically variable (Marchesiello et al., 2003), the underlying conditions for instability are forced seasonally, and possibly on longer time scales as well (Strub and James, 2000; Stegmann and Schwing, 2007; Chaigneau et al., 2009; Kurian et al., 2011). Our aim is to determine what proximate physical mechanisms modulate eddy activity on interannual and decadal frequencies, and what local and basin-scale climate processes are their most effective drivers.

Satellite observations have established the general patterns of CCS eddy activity (Kelly et al., 1998; Stegmann and Schwing, 2007; Keister and Strub, 2008). A map of the variance of relative vorticity derived from AVISO altimetry (Fig. 1A) shows an offshore band of strong eddy-scale variability. Eddy kinetic energy (EKE) has a distinct seasonal cycle, peaking in late summer/early fall (Marchesiello et al., 2003).

Few eddies are formed or propagate north of  $43^\circ\text{N}$ , possibly as a result of the detachment of the alongshore upwelling jet (Stegmann and Schwing, 2007). South of this boundary and

E-mail addresses: [andrew.davis@gatech.edu](mailto:andrew.davis@gatech.edu) (A. Davis), [edl@gatech.edu](mailto:edl@gatech.edu) (E. Di Lorenzo).

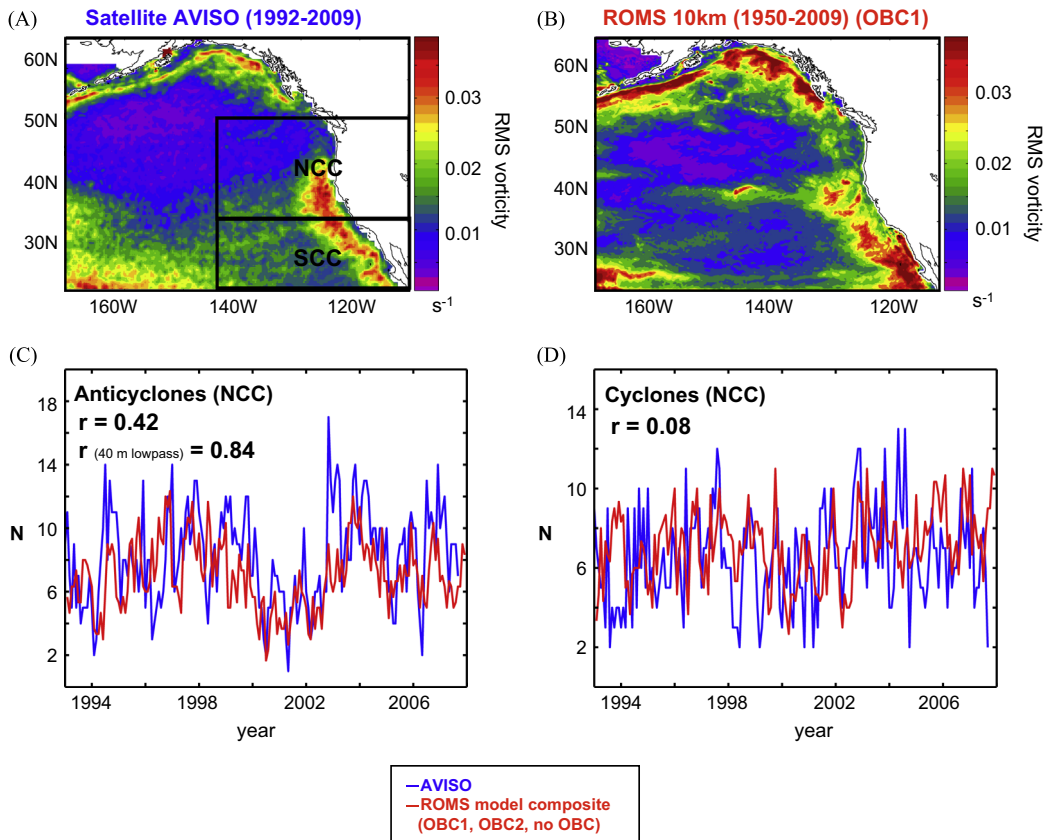


**Fig. 1.** (A) Relative vorticity variance as observed by AVISO altimetry. (B) The same variance derived from our OBC1 integration. Northern California Current (NCC) region eddy count ( $N$ ) time series derived from AVISO observations using the SSHa contour method (blue line), and a model composite from our three ROMS integrations (OBC1, OBC2, no OBC) using the  $W$  method (red line) for (C) anticyclones and (D) cyclones. (For interpretation of the references to color in this figure legend, the reader is referred to the web version of this article.)

north of the Southern California Bight (SCB), eddies are formed in a narrow region just offshore of the 1000 m isobath (Kurczyn et al., 2012). They then propagate offshore at an average rate of 1.5 km/day (roughly the same speed as short Rossby waves) (Chelton et al., 2007, 2011; Kurian et al., 2011). As eddies move westward, they tend to grow horizontally and exhibit the classical kinetic energy “length cascade” (Peltier and Stuhne, 2002). They also can become entrained in and advected meridionally by the California Current (Kurian et al., 2011).

Observational and modeling studies have confirmed that CCS eddies fall into two general categories: deep-core anticyclones (with an enstrophy maximum at roughly 400 m depth) and surface-core cyclones (Brink et al., 2000; Chereskin et al., 2000; Jeronimo and Gomez-Valdes, 2007; Kurian et al., 2011). There is a substantial bias north of the SCB towards the production of anticyclones (Stegmann and Schwing, 2007). While there is some indication that cyclone and anticyclone formation have distinct seasonal cycles (Stegmann and Schwing, 2007), other studies have concluded that there is little seasonality in the formation of all but the longest-lived eddies (Chaigneau et al., 2009; Kurian et al., 2011).

It has long been known that alongshore wind forcing generates the distribution of surface mesoscale energy in the CCS on seasonal time scales (Paressierra et al., 1993). There is also a body of work indicating that CCS eddies are formed as a result of both baroclinic instability within the poleward-flowing undercurrent and surface velocity shearing (Chereskin et al., 2000; Cornuelle et al., 2000; Marchesiello et al., 2003; Jeronimo and Gomez-Valdes, 2007). Eddy activity may also be modulated by the spatial variability of the alongshore upwelling jet (Barth et al., 2000).

Cyclones are also associated with local vertical mixing, and while they may reduce overall productivity in EBC's (Gruber et al., 2011), by bringing nutrients into the euphotic zone they can also serve as local “hot spots” for phytoplankton growth (McGillicuddy et al., 2007). Anticyclones, in contrast, are more effective in transporting tracers offshore (Cornuelle et al., 2000; Combes et al., 2013). The fact that cyclones and anticyclones may have distinct forcing mechanisms, mixing properties, ecosystem roles, and spatial distributions necessitates an approach that considers them separately.

The short length of satellite data has generally made a comparison between eddy observations and basin-scale climate indices difficult, but there have been some attempts to tie mesoscale activity to individual climate events. Keister and Strub (2008) used wavelet analysis of satellite-derived SSHa to quantify eddy kinetic energy. They found that EKE increased in the fall preceding the 1997/1998 and 2002/2003 El Niño events, but was then suppressed the following winter. In the case of the 1997/1998 event, energy did not return to its mean state until mid-2001. The 2002/2003 event had a weaker effect on EKE, possibly due to stronger teleconnected alongshore winds. They also reported a weakly significant correlation between EKE and the Pacific Decadal Oscillation, associated with low-frequency stratification anomalies and attendant available potential energy (APE) modulation.

In this study, three realizations of a North Pacific Ocean model hindcast from 1950 to 2008 were employed to determine what fraction of eddy variance was forced externally. The atmospheric forcing dynamics and accompanying ocean processes that lead to this deterministic response were then diagnosed. In Davis and Di Lorenzo (2015), we concluded that coastal-trapped wave (CTW)

energy associated with ENSO (and therefore the ENSO remote signal) was largely attenuated north of this SCB. For this reason, in this work the CCS was divided into two regions: a Northern region between 35°N and 50°N (NCC), and a Southern region between 25°N and 35°N degrees (SCC) (Fig. 1A).

**Section 2** will review the Regional Ocean Modeling System (ROMS) configuration and the special time-dependent boundary condition. **Section 3** details our methods for eddy detection, and in **Section 4** analysis is presented both of eddy variability and its external forcing in the Northern California Current. **Section 5** does the same for the Southern California Current. **Section 6** examines these results in context, as well as suggest avenues for further study.

## 2. Model configuration

This work employs a Northeastern Pacific regional hindcast from 1950 to 2008 on a 10 km resolution grid integrated by the Regional Ocean Modeling System (ROMS) (Haidvogel et al., 2008), identical to the configuration used in Davis and Di Lorenzo (2015). ROMS is an eddy-resolving ocean model that solves the incompressible primitive equations. Of particular importance in studies of the CCS is its use of terrain-following coordinates, which allow for more accurate bottom topography effects in coastal environments (Schepetkin and McWilliams, 2003). An alternate ROMS configuration was also used to successfully diagnose CCS eddy statistics and properties by Kurian et al. (2011). In this work, three model integrations were employed in order to separate the deterministic (forced) and intrinsic fractions of eddy variance.

At the surface are prescribed fluxes of momentum and heat derived from the National Center for Environmental Prediction (NCEP) Reanalysis II (Kalnay et al., 1996). The model domain has three open ocean boundaries employing a radiation boundary condition (Marchesiello et al., 2003) allowing disturbances to propagate out of the model computational domain. Two out of three of these model integrations also include a nudging to time-dependent changes at the open boundary derived from the long-term hindcast of the Ocean Model of the Earth Simulator (OFES)—a global eddy-resolving model with 10 km average resolution (Masumoto et al., 2004). The OFES hindcast also makes use of NCEP surface fluxes, making it consistent with nested ROMS computations.

This OFES boundary condition (OBC) allows for the poleward propagation of equatorially originating CTWs into and around the model domain (Marchesiello et al., 2003). CTWs alter background stratification (Battisti and Hickey, 1984), and therefore may influence eddy formation. They also carry a large amount of ENSO variance (Enfield and Allen, 1979, 1982; Chelton and Davis, 1982), possibly introducing a tropical climate signal into low-frequency CCS mesoscale activity.

This model configuration is an expansion of the one used in Di Lorenzo et al. (2008, 2009), where it was used to successfully model the interannual modulation of salinity, nutrients, and chlorophyll in the central and eastern North Pacific. Two of our model simulations include the OFES boundary condition and its

associated ENSO variance, later referred to as “OBC1” and “OBC2.” OBC2 was initialized with the final month of OBC1, but subsequently forced identically, giving it a differing initial condition. A third integration employing a purely open radiative boundary condition is included as a control, denoted “no OBC.” Details of the three model integrations are given in Table 1. OBC1 and no OBC are identical to “OBC” and “no OBC,” used previously to diagnose the drivers of large scale CCS transports (Davis and Di Lorenzo, 2015).

This model configuration has been shown to capture the observed modulation of Northeast Pacific tracer properties (Di Lorenzo et al., 2008, 2009). Here we provide some additional analyses to quantify the degree to which this model is able to capture the spatial and temporal features of CCS eddy activity. The root-mean-square relative vorticity from the OBC1 model simulation (Fig. 1B) evinces the large-scale features of eddy variability apparent from observations (Fig. 1A). The following section will detail our methods for quantifying mesoscale eddies, but an early comparison of NCC anticyclone and cyclone count time series derived from models and observations (Fig. 1C and D) shows that not only did our model integrations reproduce the stationary statistics, but nonseasonal satellite-derived anticyclone counts are correlated with a nonseasonal model composite count (mean of counts derived from OBC1, OBC2, and no OBC) at a 99% significant  $r=0.42$ .

## 3. Eddy detection methods

There are a number of methods for counting mesoscale eddies within a given region of the ocean. A detailed analysis of the advantages and pitfalls of each is given in Kurian et al. (2011). All carry a risk of false positives, underestimations, and misdiagnosis of eddy properties (radius, strength, nonlinearity, etc.). Our principal interest is in the development of robust indices of cyclone and anticyclone activity, rather than in eddy properties. This, along with the computationally demanding approach of using three separate model runs, makes counting contours of the Okubo–Weiss parameter ( $W$ ) (Okubo, 1970; Weiss, 1991) the most attractive option for our ROMS model output (Isern-Fontanet et al., 2003; Chelton et al., 2007).  $W$  is given as the difference between the squares of the strain (normal and shear) and the vorticity (Isern-Fontanet et al., 2003).

$$W = \left( \frac{\partial u}{\partial x} - \frac{\partial v}{\partial y} \right)^2 + \left( \frac{\partial v}{\partial x} + \frac{\partial u}{\partial y} \right)^2 - \left( \frac{\partial v}{\partial x} - \frac{\partial u}{\partial y} \right)^2 \quad (1)$$

An assumption of nondivergent, planar flow allows for a simplification to

$$W = 4 \left( \left( \frac{\partial u}{\partial x} \right)^2 + \left( \frac{\partial v}{\partial x} \right) \left( \frac{\partial u}{\partial y} \right) \right) \quad (2)$$

For the most effective characterization of mesoscale activity,  $W$  was computed with spatial-highpassed surface monthly mean  $u$  and  $v$ . This highpass was achieved by employing a circular spatial running mean of 200 km diameter to create an effectively lowpassed field, which was then subtracted from the full record. The resulting highpassed velocity fields were interpolated

**Table 1.** The three Northeast Pacific ROMS integrations employed.

Name	Resolution	Forcing	Boundary condition	Initialization
OBC 1	10 km w/30 vertical levels	NCEP reanalysis II	Radiative w/nudging to OFES	After spin-up from rest
OBC 2	10 km w/30 vertical levels	NCEP reanalysis II	Radiative w/nudging to OFES	With final record of OBC 1
No OBC	10 km w/30 vertical levels	NCEP reanalysis II	Radiative w/nudging to OFES	After spin-up from rest

to a resolution of 5 km in order to lessen potential noise from finite-differencing. To develop eddy count time series we summed the number of occurrences of a specific closed contour within the field. We chose a contour that gave us counts in agreement with previous observations, visual inspection, and counts derived from continuous-contouring schemes. Eddy polarity was determined using the depth of the vorticity maximum and the sign of a similarly highpassed SSHa field at the eddy center.

The  $W$ -contouring method has a well-documented bias toward false positives, with other mesoscale and sub-mesoscale features counted as eddies (Chaigneau et al., 2008). For this reason, we included a mechanism to exclude features that are insufficiently circular, similar to that of Kurian et al. (2011). This requires the calculation of the ratio of the variance of a contour from a circle of its average radius to the area of this circle. If this “shape error” exceeds 35%, the contour is excluded from the eddy count. In practice, the interannual variability of eddies tended to be insensitive to shape error criteria between 20% and 50%.

AVISO altimeter data was also employed in order to validate the model-derived eddy-count time series. Although an assumption of geostrophy would allow for computation of  $W$  contours from SSHa, the low resolution of the data (around 30 km) means that the three finite differencings required would likely generate excessive noise (Chelton et al., 2011) and possibly mask some small eddies. Here we counted closed contours of spatial-highpassed SSHa (Stegmann and Schwinger, 2007; Chaigneau et al., 2008; Chelton et al., 2011) and included a more lenient shape error criterion of 45%.

Correlation analysis is used extensively throughout this work, with time series of varying lengths and respective autocorrelations. Significance was determined using a Monte Carlo method

similar to one described in Di Lorenzo et al. (2009). PDF's of correlation coefficients used for comparison were computed with two sets of 3000 realizations of red-noise time series. These red-noise time series had identical lengths and autoregression coefficients to those of the original time series being correlated. The original correlation coefficient was then compared to this PDF to determine percent significance.

#### 4. NCC eddy variability

##### 4.1. Eddy count statistics (NCC)

Using the  $W$  eddy-count method described in Section 3, we developed eddy count time series from each of the three integrations in the NCC range. These time series share a substantial amount of variance. The three respective correlations between nonseasonal monthly counts derived from the three model runs in anticyclones and cyclones were averaged, yielding  $r=0.30$  for anticyclones and  $r=0.22$  for cyclones, indicating a substantial portion of shared (i.e. deterministic) variance.

Comparison between a nonseasonal composite eddy count time series derived from all three integrations and nonseasonal eddy counts derived from AVISO satellite altimetry (using the SSHa contouring method) (Fig. 1C and D) shows that the stationary statistics are reproduced. The correlation between observations and the composite anticyclone count is  $r=0.42$ , indicating substantial agreement. The corresponding value for cyclones is much lower, at  $r=0.08$ , but this is consistent with the increased intrinsic variance in cyclones found in the ensemble. In order to validate

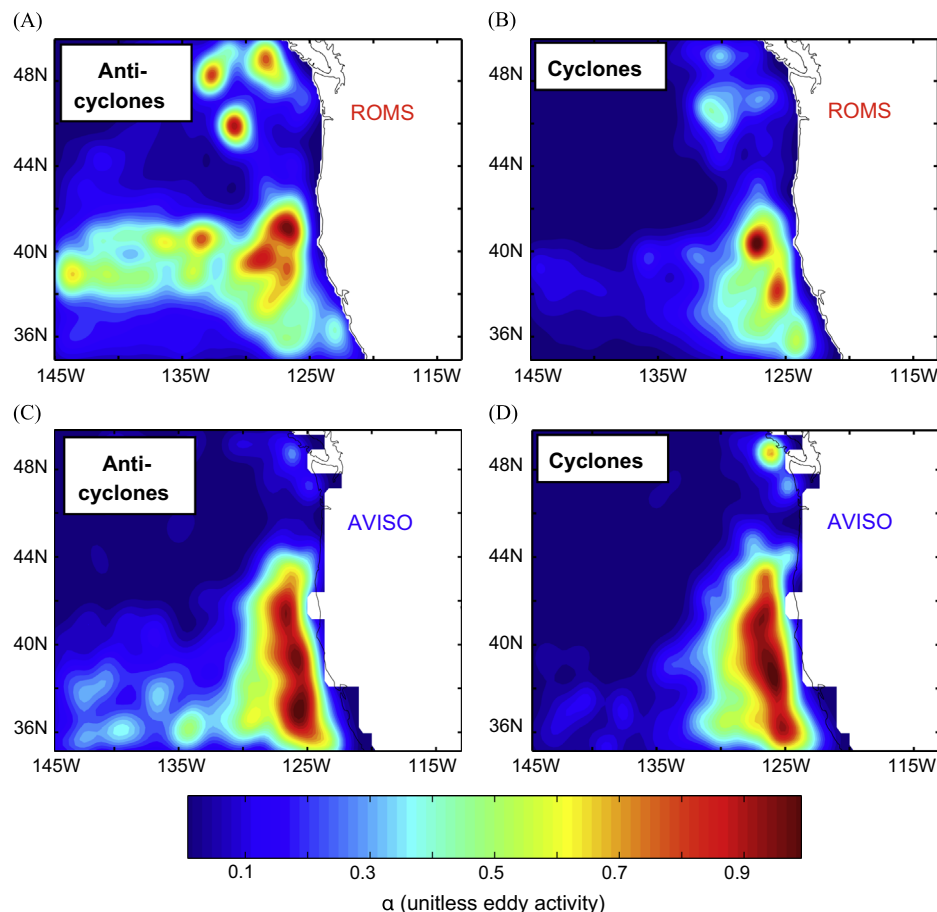


**Fig. 2.** Composite maps of ROMS-derived eddy activity ( $\alpha$ ) in the NCC region for (A) anticyclones and (B) cyclones. Corresponding maps of eddy activity from AVISO altimetry for (C) anticyclones and (D) cyclones.

the spatial patterns of model eddy formation, we developed contour plots of eddy activity by placing normal distributions at each counted eddy location and taking the time mean, providing a probabilistic view of eddy spatial distribution (Fig. 2A and B). Comparison with maps of eddy activity derived similarly from AVISO SSHa data (Fig. 2C and D), shows a general agreement in areas of eddy concentration, but with some significant differences. Both indicate that eddy activity is strongest in a region between 100 and 700 km offshore and south of 43°N, but modeled eddies are most concentrated in the northern half of this range. Model- and observation-derived maps, especially for anticyclones, both show a strong pattern of offshore propagation, but the latitudinal axis along which eddies detach differs. AVISO data shows distant offshore eddies along 37°N, while modeled eddies are confined to an axis of 40°N. In both cases, this propagation supports a hypothesis that eddies have little impact on the mean flow, and that an approach that treats eddy formation as a forced, linear process is appropriate.

Eddy counts were also examined in frequency space. Individual model run anticyclone and cyclone spectra were computed using three 20-year subsamples, along with a model composite (computed as the mean of the three model spectra) (Fig. 3A and B). Our null hypothesis—a red noise spectrum with a decorrelation time scale of 3 months—is plotted at the 99% significance level. Both anticyclones and cyclones evince a strongly significant peak at a yearly frequency, indicating that both have a robust seasonal cycle.

All other significant frequencies are within a band bounded on the high end by  $0.3 \text{ yr}^{-1}$  (periods of 40 months or more). Variance within this band is referred to throughout the remainder of this work as “low-frequency.” Based on these spectra, we determine that anticyclones have more low-frequency power (26% low-frequency; 12% seasonal), whereas cyclones have more seasonal variability (17% low-frequency; 16% seasonal). All three model runs (in gray) were plotted in the same color to show that not only do they have similar low-frequency power, but evince no notable differences at all. Most significantly, the spectra of OBC1 and OBC2 do not differ substantially from no OBC (the run employing a purely climatological boundary condition). This suggests that in the NCC, equatorial CTW variance does not play a role in low-frequency eddy modulation.

To further validate the model representation of NCC eddy variance, we compared the respective model composite seasonal cycles of cyclones and anticyclones and found that both evince the canonical late summer/early fall peak in eddy activity (Kelly et al., 1998; Strub and James, 2000; Kurian et al., 2011).

Eddy count time series were detrended, lowpassed (containing periods longer than 40 months), and normalized (to a variance of 1) to isolate modulations of interest (Fig. 3C and D). Correlations between individual runs and composites indicate that 25–35% of low-frequency variance in anticyclones is deterministic. Cyclone count correlations are somewhat lower; only 10–25% of cyclone variance is shared.

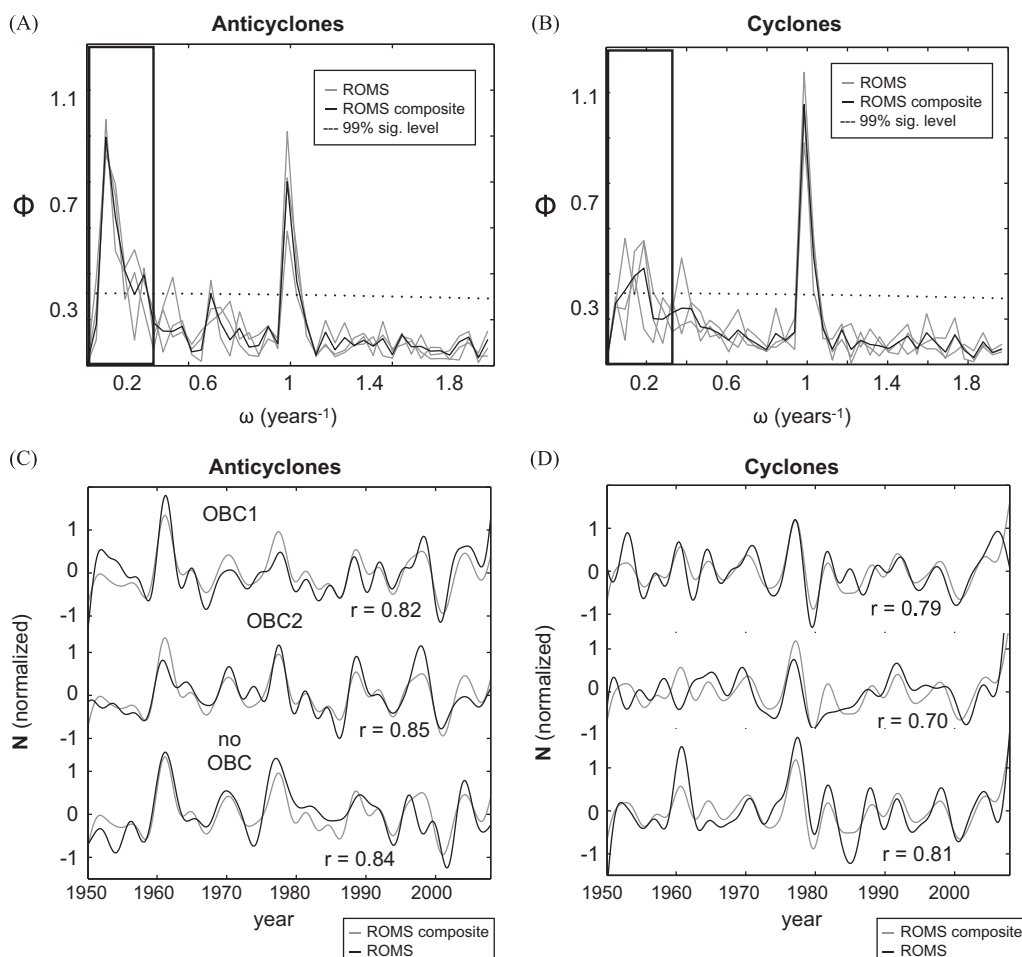


**Fig. 3.** NCC eddy count spectra ( $\Phi$ ) of 3 individual ROMS runs (OBC1, OBC2, no OBC; gray lines) and a composite spectrum (black line) for (A) anticyclones and (B) cyclones. The significant frequencies boxed in black are lowpass filtered to give eddy count time series ( $N$ ) of (C) anticyclones and (D) cyclones, for individual model runs (black lines), and a model composite (gray lines).

Lagged correlations between model composite lowpassed cyclone and anticyclone counts reach a maximum of  $r=0.73$  with cyclones leading by 4 months. On the assumption that this model composite eddy count is the optimum representation of the driven component of eddy variance, this high correlation indicates that they likely share a source of forcing on interannual (rather than just seasonal) time scales. Although considering cyclones and anticyclones separately has been vital in validating model eddy counts and in establishing their respective fractions of deterministic and intrinsic variance, they are likely forced by similar means.

#### 4.2. Physical mechanisms of eddy formation (NCC)

Eddy variability in the CCS has been theorized to be driven both by large-scale changes in the baroclinic structure (specifically the vertical stratification in the upper ocean), as well as barotropic modulation of the large-scale flow (Chereskin et al., 2000; Cornuelle et al., 2000; Marchesiello et al., 2003; Jeronimo and Gomez-Valdes, 2007). For this reason, we developed two indices of eddy formation, representing both depth-averaged (barotropic) and depth-dependent (baroclinic) components. To determine from what area these indices should be drawn, we computed maps (derived as detailed in Section 4.1) of late summer eddy activity (Fig. 4A and B), shown in our model (in agreement with observations) to be the season in which most eddies are formed.

The barotropic index was derived from a spatial mean of anomalous alongshore currents derived from each of our model outputs, depth-averaged to 400 m to ensure the capture of deep-core anticyclone formation. The record was also horizontally lowpassed at 200 km in order to remove any eddy signal. The area over which this mean was taken was an alongshore region between 36°N and 44°N (Fig. 4A). This index correlates with the lowpassed model composite anticyclone counts at  $r=0.5$  (Fig. 4C).

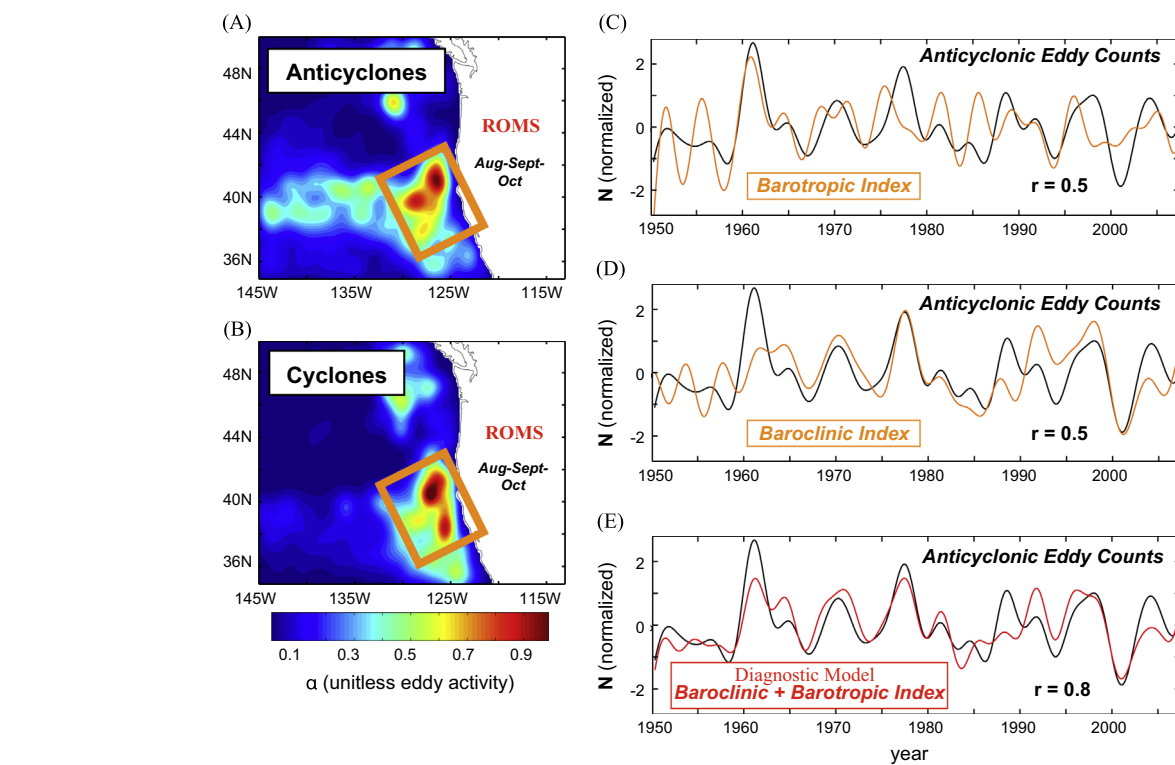


**Fig. 4.** Model composite maps of late summer/early fall (A) anticyclone and (B) cyclone activity ( $\alpha$ ) in the NCC region along with the areas of physical index averaging (overlaid in orange). The lowpass filtered model composite anticyclonic eddy counts (black lines) compared with (c) the filtered composite barotropic index (orange line), (D) the filtered composite baroclinic index (lagged at 9 months; orange line), and (E) the combined diagnostic model (red line). (For interpretation of the references to color in this figure legend, the reader is referred to the web version of this article.)

The baroclinic index was derived based on the assumption that eddies, especially anticyclones, are formed partially as the result of instabilities within the poleward-flowing undercurrent. This boundary is generally taken as isopycnal 26.5. Anomalous available potential energy should be strongly related to the stratification anomaly, and thus the distance between neighboring isopycnals. The index was computed by calculating the gradient of horizontally lowpassed isopycnal depth in the vertical dimension about 26.5 and taking a horizontal mean in the observed area of eddy formation. This index also correlates with the lowpassed model composite anticyclone counts at  $r=0.5$  (Fig. 4D) at a lag of 9 months.

Barotropic and baroclinic indices show no significant correlations for lags of up to one year, indicating that they are largely orthogonal and independent. Least-squares analysis provides correlations and lags of maximum correlation between each of these indices and eddy count time series ( $r=0.5$  at 9 months for the baroclinic index;  $r=0.5$  at 0 months for the barotropic index). These correlations can then be employed as weighting coefficients in order to combine baroclinic and barotropic indices into a single diagnostic model of potential eddy activity. Correlation of a lowpassed composite (a mean of from all three model simulations) of this diagnostic model with lowpassed composite anticyclone count is a 99% significant  $r=0.8$  (Fig. 4E). Although cyclones have a smaller fraction of deterministic variance (only 10–15%), this index also correlates well with a lowpassed composite cyclone count at  $r=0.7$ . Additionally, this index correlates with individual runs at between  $r=0.6$  and 0.8 for anticyclones and between 0.4 and 0.6 for cyclones.

#### 4.3. Wind forcing of eddy variability

Spectral analysis indicated that the time-dependent OFES boundary condition added little low-frequency variance to modeled eddy counts. Therefore equatorial CTW influence on NCC eddy activity is

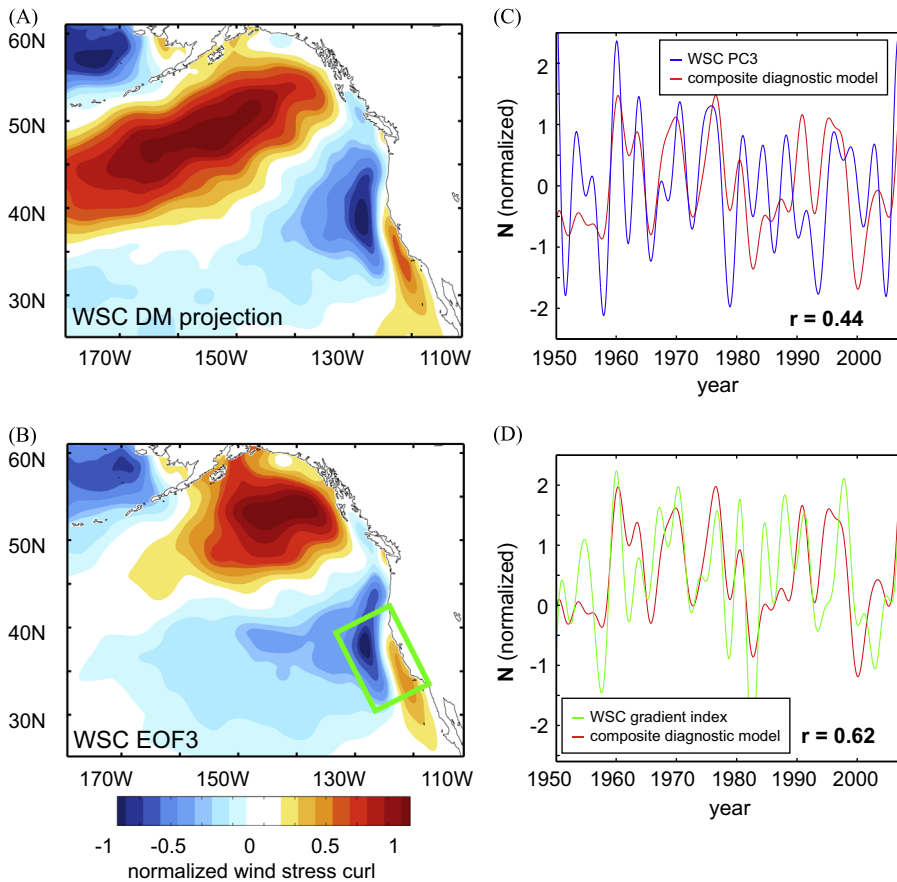


**Fig. 5.** (A) The projection of the composite diagnostic model (DM) onto Northeastern Pacific NCEP wind stress curl (WSC) with spatial variance normalized to 1. (B) The normalized 3rd EOF of Northeastern Pacific NCEP wind stress curl, with the area over which the wind stress curl gradient index is averaged (green box). (C) The composite diagnostic model (red line) compared with a lowpass filtered time series of the corresponding 3rd principal component of WSC (blue line). (D) The composite diagnostic model (red line) compared with the lowpass filtered wind stress curl gradient index (green line). (For interpretation of the references to color in this figure legend, the reader is referred to the web version of this article.)

minimal; forcing is most likely local and wind-driven. To determine what wind patterns most effectively drive eddy variance, we projected our three-run composite of the diagnostic model onto each point of Northeast Pacific NCEP wind stress curl anomalies. The pattern recovered (Fig. 5A) has a cross-shelf dipolar shape across the NCC region, as well as pronounced structure to the north and in the offshore. The patterns of the respective projections of the separate barotropic and baroclinic indices (not shown) are extremely similar to this pattern, especially in the CCS region. This indicates that while these indices are independent, both are forced by the same wind stress curl gradient.

A further examination of the wind forcing patterns reveals strong similarities between this pattern and the 3rd empirical orthogonal function (EOF) of Northeastern Pacific (NEP) NCEP wind stress curl (Fig. 5B). While the first two EOF's of NEP wind stress curl correspond to the Aleutian Low and the North Pacific Oscillation (NPO), respectively, this third mode has not been widely studied and is characterized by strong regional projection along the California Current. While it only represents 8% of variance across the Northeastern Pacific, locally (in the NCC), it accounts for 50% of variance. This 3rd principal component (lowpassed at 40 months) correlates at  $r=0.44$  with our lowpassed composite diagnostic model (Fig. 5C). This relatively low correlation suggests that the regional component of the wind pattern plays an important role, necessitating an index of large-scale cross-shelf wind stress curl gradients in the CCS region (overlaid onto Fig. 5C). Correlation between a 40-month lowpass of this index and the lowpassed composite diagnostic model is a 99% significant 0.62. We computed lagged correlations between

composite lowpassed eddy counts and the third principal component of NEP wind stress curl ( $r=0.46$  at lag=9 months) as well as the curl gradient index ( $r=0.50$  at lag=9 months). The fraction of variance explained by these wind indices (25%) is comparable to the proportion of driven variance in eddy counts (25–35% for anticyclones; 10–25% for cyclones), strongly suggesting that local wind variability drives eddy activity on interannual and decadal scales, just as it does seasonally. Correlations between these wind indices and eddy counts are not as high as those between eddy counts and our diagnostic model, indicating that a portion of variance of barotropic and baroclinic structures is not derived from wind stress, but either intrinsic or forced by other means.

## 5. Eddy count statistics (SCC)

Model composite maps of SCC eddy activity from both model runs and observations (Fig. 6) evince noticeable inconsistencies, possibly reflecting some of the biases in relative vorticity found near the southeast boundary of the ROMS integration (Fig. 1A). Observational records show strong eddy activity extending further towards the SCB and further offshore.

Spectra from the OBC1 and OBC2 runs for anticyclones and cyclones (Fig. 7A and B) show much less seasonality than the NCC, but have a narrow band of significant low frequencies, once again bounded at 0.3 cycles per year. As in the NCC, these two runs do not noticeably differ. In contrast to the NCC, this low-frequency band is much diminished in the no OBC run (Fig. 7C and D), whose spectra conform roughly to red noise. The lack of any band of significant

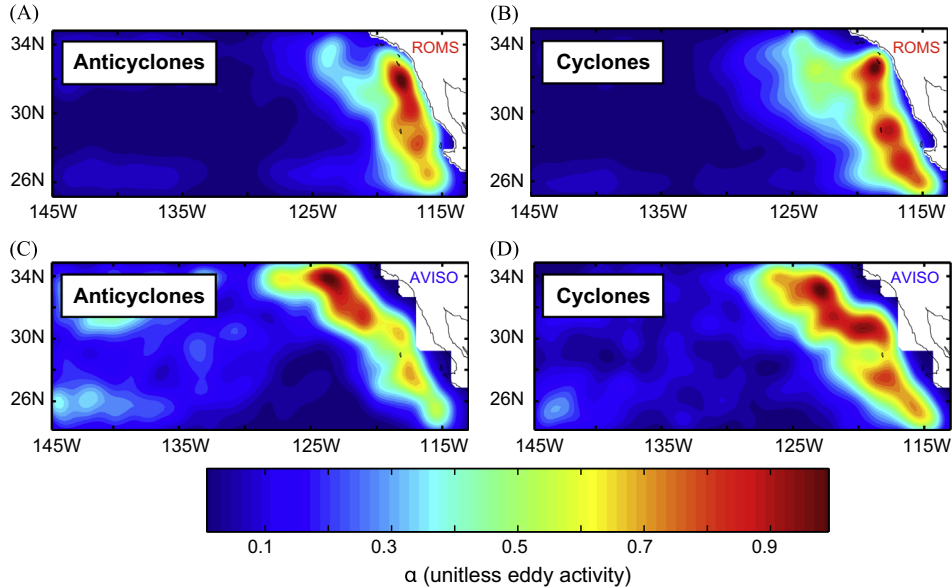


**Fig. 6.** Model composite maps of ROMS-derived eddy activity ( $\alpha$ ) for (A) anticyclones and (B) cyclones in the Southern California Current (SCC) region. (C and D) Maps of eddy activity from AVISO altimetry are also computed for anticyclones and cyclones, respectively.

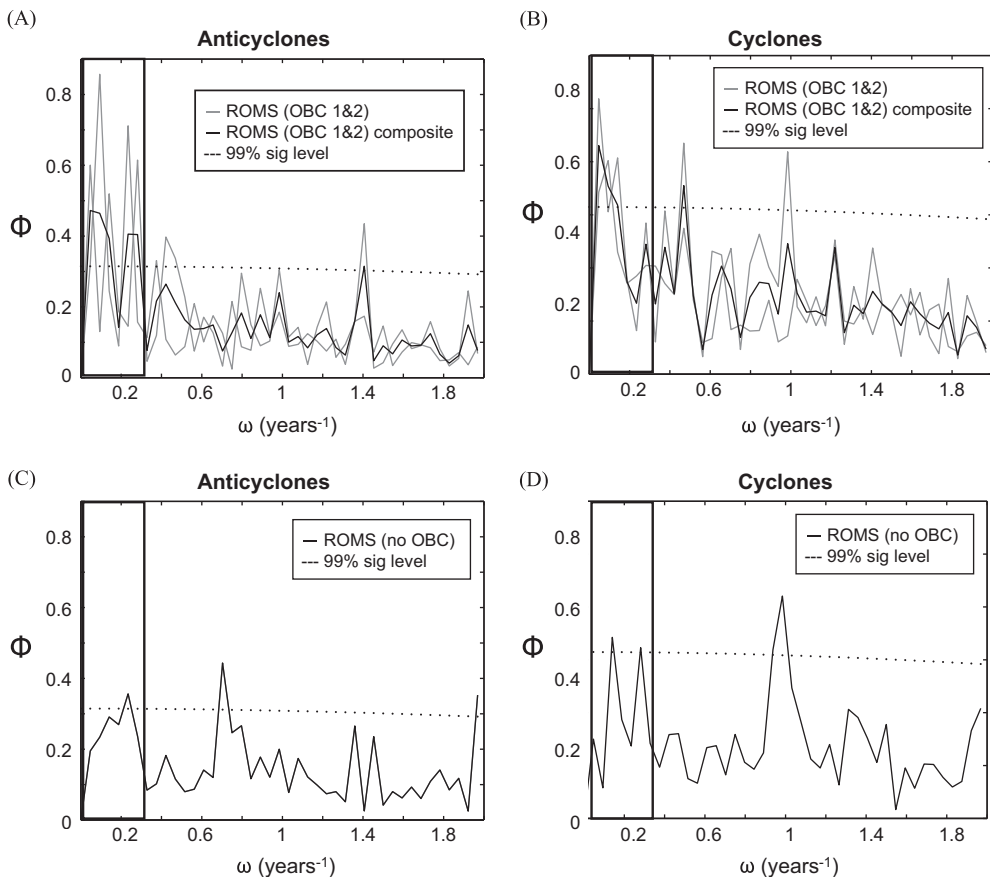


**Fig. 7.** SCC region eddy count spectra ( $\phi$ ) for the OBC1 and OBC2 ROMS runs (gray lines) and a composite spectrum from the two (black lines) for (A) anticyclones and (B) cyclones. (C and D) SCC region eddy count spectra ( $\phi$ ) for the no OBC run (black line) for anticyclones and cyclones, respectively.

frequencies in this run implies that it is the OFES boundary condition that contributes the significant low-frequency variance to the OBC1 and OBC2 runs, likely by means of CTW activity.

Low correlations between 40-month lowpassed eddy count time series and model composites (Fig. 8) suggest that only around 10% of low-frequency anticyclone variance is shared, while cyclone variance

is virtually completely intrinsic. This is consistent with the spectral characterization of SCC eddy activity as largely a red-noise process.

Our explanation for the increased intrinsic variance in modeled SCC eddy counts is as follows. Seasonal maps of SCC anticyclone (Fig. 9A) and cyclone (Fig. 9B) activity show very little offshore propagation, indicating that modeled eddies are effectively

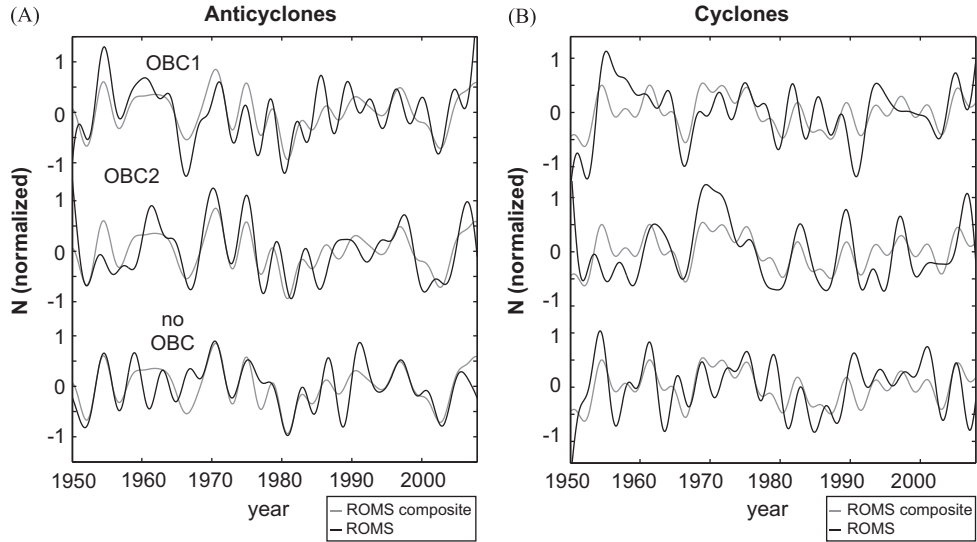


**Fig. 8.** 40-month lowpass filtered SCC regional eddy count ( $N$ ) time series of (A) anticyclones and (B) cyclones, for individual model runs (black lines), and a model composite (gray lines).

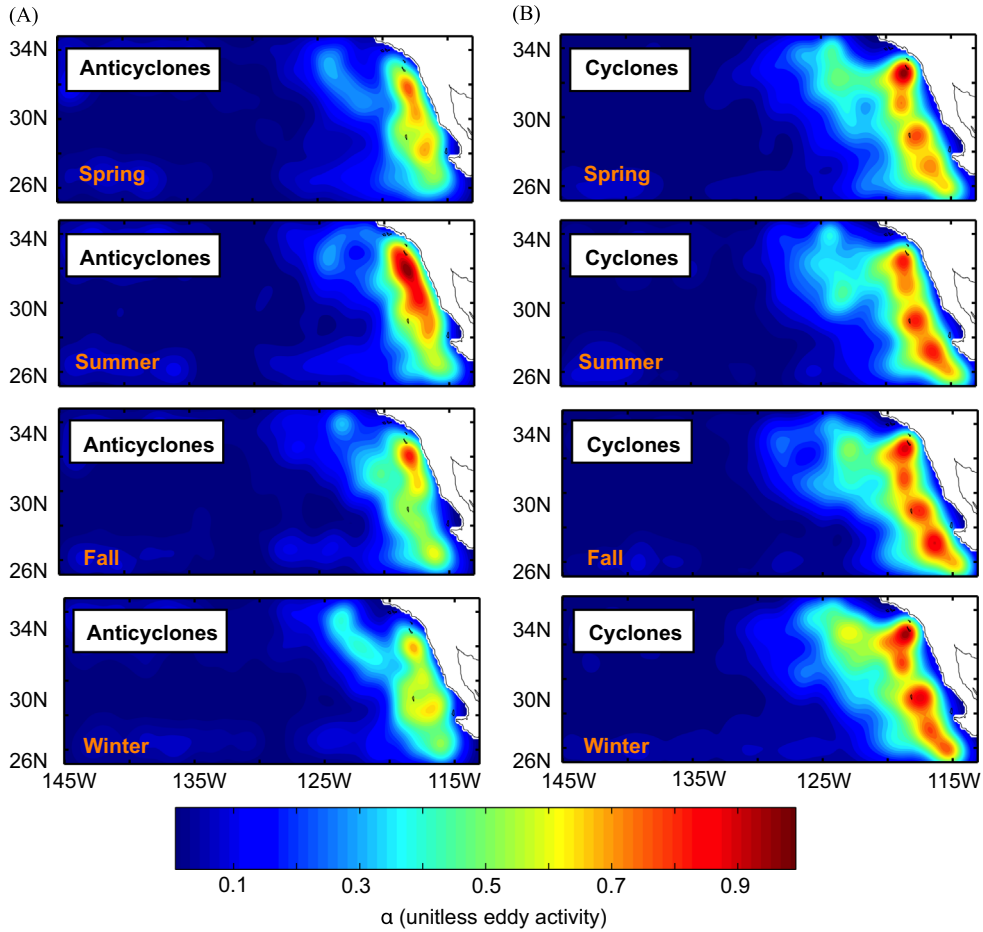


**Fig. 9.** Seasonal model composite maps of SCC regional eddy activity (●) for (A) anticyclones and (B) cyclones.

entrained in recirculating currents. This prolonged residence time for SCC eddies means that they have a much greater effect on the background mean, leading to feedbacks, nonlinearity, and unpredictability. This coupling between large-scale and mesoscale properties would preclude the linear, forced response seen in the NCC.

## 6. Conclusion

These results are strong evidence that in the NCC, local wind variability regulates mesoscale eddy activity on interannual and decadal time scales, just as it does seasonally. While there remains a significant amount of intrinsic variance on these time scales,

the deterministic component is composed of both barotropic and baroclinic variability in the large-scale flow, both of which are modulated by wind stress curl gradients. In the SCC, there is very little forced variance in evidence. The recirculation and attendant feedbacks add noise and intrinsic variability which dominate any deterministic component.

In Davis and Di Lorenzo (2015), we showed that the influence of coastal trapped waves on large-scale SSHa and alongshore currents diminished north of the Southern California Bight. It was largely for this reason that we split our two areas of study along this latitude. We investigated the possibility that ENSO impacts mesoscale eddy activity (as reported by Keister and Strub (2008)), and results were mixed. SCC anticyclone and cyclone counts coming from our “OBC1” model run showed weakly significant negative correlations with Niño 3.4 at a lag of 6 months. Eddy counts from our “no OBC” run were uncorrelated with Niño 3.4 (as expected, given its time-independent boundary condition) but those from “OBC2” were, as well. With only one of the two OBC runs evincing an ENSO signal in eddy counts, we can only say that there is conflicting evidence of tropical influence on CCS mesoscale activity.

It should be noted that although our model simulations could reproduce the stationary statistics, broad spatial patterns, and (in the cases of NCC anticyclones) interannual variability of CCS eddy activity as derived from AVISO altimetry, there is ample cause to suspect dissimilarity with actual eddy activity. Modeled NCC eddies propagate offshore further north than in observations, and modeled SCC eddies propagate less effectively. This may add artificial intrinsic variance to modeled SCC eddy counts. AVISO itself may not resolve some nearshore mesoscale activity, limiting the scope of model validation. In addition, the coarse NCEP reanalysis winds used to force our model cannot resolve fine-scale wind variability, which may also play a role in eddy formation.

In addition to caveats concerning the agreement of our model with observations, there are several limitations inherent in the largely theoretical approach taken here. Although our barotropic and baroclinic indices were based on mechanisms widely theorized to underly eddy formation, we have not attempted to describe the process in detail. A full dynamical approach to this question could establish precisely how wind stress curl anomalies contribute variance to instability along both these pathways. We leave this to future studies.

The treatment of mesoscale activity as a forced, rather than coupled, process is also inherently limiting, especially in our study of the SCC. The relatively simple correlation analysis used here is not suited to the strongly nonlinear nature of SCC eddy processes. A more sophisticated modeling approach is needed if the interplay of atmospheric forcing, CTW forcing, large-scale flow, and mesoscale activity is to be effectively diagnosed.

We have also made no attempt to quantify the mixing associated with surface cyclones and deep-core anticyclones, which is of primary importance in establishing the impacts of these low-frequency mesoscale modulations on CCS ecosystems.

## Acknowledgments

This study was supported by the National Science Foundation (NSF OCE-0550266, POBEX Project NSF-GLOBEC OCE-0815280 and NSF CCE-LTER).

## References

- Barth, J.A., Pierce, S.D., Smith, R.L., 2000. A separating coastal upwelling jet at Cape Blanco, Oregon and its connection to the California Current System. *Deep-Sea Res. II* 47, 783–810.
- Battisti, D.S., Hickey, B.M., 1984. Application of remote wind-forced coastal trapped wave theory to the Oregon and Washington coasts. *J. Phys. Oceanogr.* 14, 887–903.
- Brink, K.H., Beardsley, R.C., Paduan, J., Limeburner, R., Caruso, M., Sires, J.G., 2000. A view of the 1993–1994 California Current based on surface drifters, floats, and remotely sensed data. *J. Geophys. Res.—Oceans* 105, 8575–8604.
- Chaigneau, A., Eldin, G., Dewitte, B., 2009. Eddy activity in the four major upwelling systems from satellite altimetry (1992–2007). *Prog. Oceanogr.* 83, 117–123.
- Chaigneau, A., Gizolme, A., Grados, C., 2008. Mesoscale eddies off Peru in altimeter records: identification algorithms and eddy spatio-temporal patterns. *Prog. Oceanogr.* 79, 106–119.
- Chelton, D.B., Davis, R.E., 1982. Monthly mean sea-level variability along the west coast of North America. *J. Phys. Oceanogr.* 12, 757–784.
- Chelton, D.B., Schlax, M.G., Samelson, R.M., 2011. Global observations of nonlinear mesoscale eddies. *Prog. Oceanogr.* 91, 167–216.
- Chelton, D.B., Schlax, M.G., Samelson, R.M., de Szoeke, R.A., 2007. Global observations of large oceanic eddies. *Geophys. Res. Lett.* 34, L15606, <http://dx.doi.org/10.1029/2007gl030812>.
- Chereskin, T.K., Morris, M.Y., Niiler, P.P., Kosro, P.M., Smith, R.L., Ramp, S.R., Collins, C.A., Musgrave, D.L., 2000. Spatial and temporal characteristics of the mesoscale circulation of the California Current from eddy-resolving moored and shipboard measurements. *J. Geophys. Res.—Oceans* 105, 1245–1269.
- Combes, V., Chenillat, F., Di Lorenzo, E., Riviere, P., Ohman, M.D., Bograd, S.J., 2013. Cross-shore transport variability in the California Current: Ekman upwelling vs. eddy dynamics. *Prog. Oceanogr.* 109, 78–89.
- Cornuelle, B.D., Chereskin, T.K., Niiler, P.P., Morris, M.Y., Musgrave, D.L., 2000. Observations and modeling of a California undercurrent eddy. *J. Geophys. Res.—Oceans* 105, 1227–1243.
- Davis, A.M., Di Lorenzo, E., 2015. Interannual forcing mechanisms of California Current transports II: Meridional Currents. *Deep-Sea Res. II (CCE-LTER Special Issue)* 112, 31–41.
- Di Lorenzo, E., et al., 2009. Nutrient and salinity decadal variations in the central and eastern North Pacific. *Geophys. Res. Lett.* 36, L14601, <http://dx.doi.org/10.1029/2009gl038261>.
- Di Lorenzo, E., et al., 2008. North Pacific Gyre Oscillation links ocean climate and ecosystem change. *Geophys. Res. Lett.* 35, L08607, <http://dx.doi.org/10.1029/2007gl032838>.
- Fukumori, I., Lee, T., Cheng, B., Menemenlis, D., 2004. The origin, pathway, and destination of Nino-3 water estimated by a simulated passive tracer and its adjoint. *J. Phys. Oceanogr.* 34, 582–604.
- Gruber, N., Frenzel, H., Doney, S.C., Marchesiello, P., McWilliams, J.C., Moisan, J.R., Oram, J.J., Plattner, G.K., Stolzenbach, K.D., 2006. Eddy-resolving simulation of plankton ecosystem dynamics in the California Current System. *Deep-Sea Res. I* 53, 1483–1516.
- Gruber, N., Lachkar, Z., Frenzel, H., Marchesiello, P., Munnich, M., McWilliams, J.C., Nagai, T., Plattner, G.K., 2011. Eddy-induced reduction of biological production in eastern boundary upwelling systems. *Nat. Geosci.* 4, 787–792.
- Haidvogel, D.B., et al., 2008. Ocean forecasting in terrain-following coordinates: Formulation and skill assessment of the Regional Ocean Modeling System. *J. Comput. Phys.* 227, 3595–3624.
- Isern-Fontanet, J., Garcia-Ladona, E., Font, J., 2003. Identification of marine eddies from altimetric maps. *J. Atmos. Ocean. Technol.* 20, 772–778.
- Jeronimo, G., Gomez-Valdes, J., 2007. A subsurface warm-eddy off northern Baja California in July 2004. *Geophys. Res. Lett.* 34, L06610, <http://dx.doi.org/10.1029/2006gl028851>.
- Kalnay, E., et al., 1996. The NCEP/NCAR 40-year reanalysis project. *Bull. Am. Meteorol. Soc.* 77, 437–471.
- Keister, J.E., Strub, P.T., 2008. Spatial and interannual variability in mesoscale circulation in the northern California Current System. *J. Geophys. Res.—Oceans* 113, C04015, <http://dx.doi.org/10.1029/2007jc004256>.
- Kelly, K.A., Beardsley, R.C., Limeburner, R., Brink, K.H., Paduan, J.D., Chereskin, T.K., 1998. Variability of the near-surface eddy kinetic energy in the California Current based on altimetric, drifter, and moored current data. *J. Geophys. Res.—Oceans* 103, 13067–13083.
- Kurczyn, J.A., Beier, E., Lavin, M.F., Chaigneau, A., 2012. Mesoscale eddies in the northeastern Pacific tropical-subtropical transition zone: statistical characterization from satellite altimetry. *J. Geophys. Res.—Oceans* 117, C10021, <http://dx.doi.org/10.1029/2012jc007970>.
- Kurian, J., Colas, F., Capet, X., McWilliams, J.C., Chelton, D.B., 2011. Eddy properties in the California Current System. *J. Geophys. Res.—Oceans* 116, C08027, <http://dx.doi.org/10.1029/2010jc006895>.
- Marchesiello, P., McWilliams, J.C., Shchepetkin, A., 2003. Equilibrium structure and dynamics of the California Current System. *J. Phys. Oceanogr.* 33, 753–783.
- Masumoto, Y., et al., 2004. A fifty-year eddy-resolving simulation of the World Ocean—preliminary outcomes of OFES (OGCM for the Earth Simulator). *J. Earth Simul.* 1, 35–36.
- McGillicuddy, D.J., et al., 2007. Eddy/wind interactions stimulate extraordinary mid-ocean plankton blooms. *Science* 316, 1021–1026.
- Okubo, A., 1970. Horizontal dispersion of floatable particles in vicinity of velocity singularities such as convergences. *Deep-Sea Res.* 17, 445–454.
- Paressierra, A., White, W.B., Tai, C.K., 1993. Wind-driven coastal generation of annual mesoscale eddy activity in the California Current. *J. Phys. Oceanogr.* 23, 1110–1121.

- Peltier, W.R., Stuhne, G., 2002. The upscale turbulence cascade: shear layers, cyclones and gas giant bands. In: Pearce, R.P. (Ed.), *Meteorology at the Millennium*. Academic Press, London, pp. 43–61.
- Stegmann, P.M., Schwing, F., 2007. Demographics of mesoscale eddies in the California Current. *Geophys. Res. Lett.* 34, L14602, <http://dx.doi.org/10.1029/2007gl029504>.
- Strub, P.T., James, C., 2000. Altimeter-derived variability of surface velocities in the California Current System: 2. Seasonal circulation and eddy statistics. *Deep-Sea Res. II* 47, 831–870.
- Weiss, J., 1991. The dynamics of enstrophy transfer in 2-dimensional hydrodynamics. *Physica D* 48, 273–294.